Acid-induced surface reconstruction of NiSeTe revealed by NAP-XPS

Applied Surface Science 746 (2026) 167652

Contents lists available at ScienceDirect

Applied Surface Science

journal homepage: www.elsevier.com/locate/apsusc

Full Length Article

Acid-induced surface reconstruction of NiSeTe revealed by NAP-XPS

Ashraf Abdelrahman Assadig Elameen [a,b,*], Tomáš Hrbek [c], Yevheniia Lobko [c], Viacheslav Kalinovych [c], Angelica Chiodoni [a,e], Micaela Castellino [a,e], Peter Kúš [c], Rui Gusmão [d], Zdenek Sofer [d], Andrea Lamberti [a,e]

[a] Department of Applied Science and Technology, Polytechnic University of Turin, Corso Duca degli Abruzzi, 24, 10129 Turin, Italy
[b] Department of Physical and Chemical Sciences, University of L'Aquila, via Vetoio, 67100 L'Aquila, (AQ), Italy
[c] Department of Surface and Plasma Science, Faculty of Mathematics and Physics, Charles University, V Holešovičkách 2, 180 00 Prague 8, Czech Republic
[d] Department of Inorganic Chemistry, University of Chemistry and Technology, Prague Technická 5, Prague 616628, Czech Republic
[e] Italian Institute of Technology – Advanced Materials for Sustainable Future Technologies, via Livorno, 60, 10144 Turin, Italy

ARTICLE INFO

Keywords:
NAP-XPS
NiSeTe
Acid-driven reconstruction
Oxide-free surface
TMCs

ABSTRACT

Surface activation of transition metal chalcogenides (TMCs) is commonly attributed to electrochemical reduction and defect formation under applied bias. Herein, we demonstrate that for single-crystalline NiSeTe, a significant fraction of the surface transformation typically associated with electrochemical activation instead arises from purely chemical, sulfuric acid-driven (H_2SO_4) reconstruction occurring prior to any applied potential. Near-ambient pressure X-ray photoelectron spectroscopy (NAP-XPS) is employed to monitor the evolution of pristine, acid-exposed, and washed surfaces. Acid treatment selectively removes native TeO_x species and Ni-O(H) environments, while heterogeneous sulfate-derived species collapse into a transient S(VI)-rich adlayer. Subsequent washing eliminates weakly bound sulfates and yields a chemically simplified, oxide-free NiSeTe surface with a thin, stable sulfate termination. Notably, operando, bias-controlled NAP-XPS measurements with simultaneous chronoamperometric current monitoring reveal that cathodic polarization under HER-relevant conditions does not further reduce the acid-reconstructed surface, indicating that sulfuric acid exposure already generates an oxide-free NiSeTe termination prior to electrochemical biasing. In contrast, anodic polarization under OER-relevant conditions promotes tellurium re-oxidation. These findings establish acid-driven chemical restructuring as a dominant contributor to surface activation in NiSeTe and underscore the importance of disentangling chemical and electrochemical effects in chalcogenide electrocatalysts.

1. Introduction

Transition metal chalcogenides (TMCs) have emerged as versatile platforms for electrocatalysis because their catalytic activity is governed by diverse chemical and electronic features derived from their electronic bulk structure, surface termination, defect chemistry, and the dynamic interplay between metal and chalcogen sites during operation [1–4]. Ni-based selenides and tellurides have received attention for hydrogen evolution and related interfacial reactions owing to their tunable covalency and multivalent bonding environments [5–7]. The different electronegativities, polarizabilities, and orbital sizes of Se and Te allow the Ni coordination sphere to adopt a spectrum of charge distribution patterns and metal–chalcogen hybridization strengths, making mixed-anion systems especially attractive for catalytic design [8,9]. Within this family, multinary compounds such as NiSeTe exhibit even richer complexity: their crystal structures can accommodate variable anion ordering and defect distributions, while their electronic structures offer pathways for modulating both active-site energetics and reaction intermediates [10,11].

In practice, the catalytic response is dictated predominantly by the outermost atomic layers, where chemical bonding, adsorption energetics, and charge transfer are defined. As a result, surface-localized transformations dominate apparent activity trends.

The surface chemistry of transition metal chalcogenides is rarely pristine [12]. Air exposure commonly leads to the formation of self-passivating layers composed of oxides, hydroxides, and sulfate-derived species that cover the intrinsic chalcogenide termination. However, direct NAP-XPS studies that systematically separate the pristine, acid-exposed, and post-washed surface states of Te-containing transition-metal chalcogenides remain scarce, making it difficult to distinguish

* Corresponding author at: Department of Applied Science and Technology, Polytechnic University of Turin, Corso Duca degli Abruzzi, 24, 10129 Turin, Italy.

https://doi.org/10.1016/j.apsusc.2026.167652
Received 17 April 2026; Received in revised form 2 June 2026; Accepted 22 June 2026
Available online 23 June 2026

spontaneous acid-driven reconstruction from changes induced by electrochemical bias. These surface layers can obscure intrinsic activity and, therefore, give rise to misleading interpretations of activation phenomena. Te-containing chalcogenides are particularly susceptible to such complications: Te readily forms TeO_2 or mixed TeO_x species upon air exposure [13,14], while Ni sites often oxidize to $Ni(OH)_2$ or NiO, producing complex multiphase surfaces that differ substantially from the bulk lattice [15]. These native surface layers are not inert; they dissolve, reorganize, or desorb rapidly upon contact with acidic electrolytes.

Despite this, a recurring theme in the electrocatalysis literature is the assumption that Te-bearing materials undergo self-reconstruction during electrochemical activation, yielding Te^0, Te vacancies, or Te-depleted surfaces that are purported to enhance catalytic activity [16]. For example, in 1 T′-$MoTe_2$ the HER overpotential required to sustain 10 mA cm^{-2} decreases from ~ 320 mV to ~ 178 mV when the electrode is held at cathodic bias, and the enhanced activity reverts when the bias is removed, directly linking electrochemical potential to catalytic performance [17]. While such processes may indeed occur under sufficiently high potentials (typically below -0.5 V vs RHE), much of the literature fails to rigorously distinguish between bias-induced changes and those arising from spontaneous chemical exposure.

Specifically, the direct interaction of TeO_x and NiO_x layers with acidic electrolyte can trigger rapid dissolution and restructuring even before the initial polarization cycles [18,19]. Without isolating these contributions, assigning catalytic enhancement to intrinsic electronic modifications, rather than to selective leaching or surface cleaning', remains speculative.

In this work, we address this challenge directly by investigating the intrinsic chemical activation of single crystalline NiSeTe induced solely by controlled exposure to acidic media. Using near ambient pressure X-ray photoelectron spectroscopy (NAP-XPS), we systematically track the evolution of pristine, acid-exposed, and washed surfaces under identical measurement conditions, without applying any electrochemical bias. This approach enables us to isolate proton-driven chemical processes and quantify their impact on surface composition and bonding.

By correlating the evolution of O-1 s, S-2p, Te-3d, Se-3d, and Ni-2p signals, we construct a detailed picture of the acid-driven transformation pathway. The data reveal that acid treatment selectively dissolves Te-oxide species, thins Ni-oxide/hydroxide layers, reorganizes surface sulfate environments, and transiently suppresses Se and Ni lattice signals through partial dissolution or coverage by sulfate-derived oxygen. Following rinsing, characteristic Se-chalcogenide doublets reappear, the Ni-2p region collapses into a simplified chalcogenide signature devoid of $NiO/Ni(OH)_2$, and the S-2p region develops two distinct S(VI) environments that reflect the reconstructed termination.

Collectively, these observations demonstrate that acid alone, without electrochemical bias, is sufficient to expose, reshape, and stabilize new surface terminations on NiSeTe. This mechanism reflects the need for precise characterizations before delving into the complex system of electrochemical cell where more parameters operate. For instance, numerous electrocatalysis studies report that reduction of surface oxides or creation of oxygen/chalcogen vacancies improves catalytic activity [18,19]. Defect-rich transition metal dichalcogenides, created via reduction or defect engineering, also show dramatically enhanced hydrogen evolution activity [20]. While these examples clearly show that reductive removal of surface oxides or vacancy formation can promote activity, they also highlight the importance of rigorously distinguishing such effects from acid-driven chemical transformations when interpreting electrocatalytic activation. Instead, we focus on an overlooked mechanism that operates at the earliest stages of the hydrogen evolution reaction: acid-driven surface reconstruction occurring prior to the application of any electrochemical bias. Our results demonstrate that a substantial fraction of the surface transformations frequently subsumed under the broad concept of electrochemical activation can, in fact, be explained by selective chemical dissolution of native oxides and subsequent reorganization of surface species induced solely by electrolyte contact. Recognizing and separating these chemically driven processes from true bias-induced restructuring is essential for the correct interpretation of activation phenomena in chalcogenide electrocatalysts.

Because NiSeTe readily forms surface-localized oxide and hydroxide species under ambient conditions, it is essential to disentangle chemical restructuring confined to the outermost atomic layers from deeper changes within the bulk lattice. Near-ambient pressure XPS provides precisely this capability, offering element-specific sensitivity to the removal of TeO_2, the transformation of Ni-OH species, and the redistribution of chalcogen bonding configurations that ultimately define the functional surface chemistry.

2. Experimental section

2.1. Crystal growth and structural verification

Single-crystalline NiSeTe was synthesized via a high-temperature method analogous to reported preparation routes for layered Ni [21]. Stoichiometric mixture of Ni (99.99%, 100 mesh), Se (99.999%, granules 2–4 mm), and Te (99.999%, granules 2–6 mm) corresponding to 25 g were sealed in quartz ampoule (25x100 mm) under high vacuum ($<1x10^{-3}$ Pa using oil diffusion pump and liquid nitrogen trap) by oxygen-hydrogen welding torch. Ampoule was placed in muffle furnace and heated to 1000 °C using heating rate of 1°C/min. After 6 h the ampoule was cooled to 500 °C using cooling rate of 6°C/hour and finally allowed to cool naturally to room temperature. The ampoule was opened in argon filled glovebox and formed crystals were collected.

The bulk crystal structure was confirmed via powder and single-crystal X-ray diffraction (XRD), collected on finely ground fragments and oriented crystal surfaces using Cu Kα radiation. X-ray diffraction (XRD) measurements were carried out using a Bruker D2 Phaser benchtop diffractometer (Bruker, Germany) with a Cu Kα radiation source (λ = 1.54178 Å). The diffraction patterns were acquired in the range of 2θ from 5 to 90°, at room temperature. The data were evaluated by HighScore Plus 4.9 software.

2.2. Morphology and elemental composition

The morphology and elemental composition of the as-synthesized NiSeTe were characterised by field emission scanning electron microscopy (FESEM) with field emission Tescan LYRA3 GM dual-beam microscope and Tescan MAIA3 (Tescan, Czech Republic) at an acceleration voltage of 5 kV. Elemental composition was investigated by energy-dispersive x-ray spectroscopy (EDS) (Oxford Instruments X-MaxN detector) at 20 kV acceleration voltage. For these measurements, the crystalline powder was mounted on conductive carbon tape.

To evaluate the impact of chemical activation, surface morphology and composition were examined before and after acid exposure using a Tescan Mira III SEM operating in secondary electron mode at 10 kV. Localized elemental changes were monitored via EDS using a Bruker XFlash 6|10 detector. All surface analyses were performed on both pristine and acid-treated/rinsed samples to track structural and stoichiometric evolution; corresponding SEM micrographs are provided in the Supplementary Information.

2.3. Acid exposure and washing procedure

To decouple purely chemical effects from electrochemical phenomena, no electrical potential was applied during the surface treatment. The chemical reconstruction was induced by drop-casting a 50 μL aliquot of 0.5 M H_2SO_4 onto the oriented crystal surface. The droplet was left to react for 30 min under ambient conditions before being carefully wicked away with lint-free paper.

Samples were then processed under two distinct protocols:

Acid-exposed (unwashed): The sample was immediately transferred to the XPS vacuum load-lock to monitor the transient surface chemistry and the presence of sulfate-derived species.
Acid-treated and washed: A separate set of samples, following the 30-minute acid exposure, was thoroughly rinsed with ultrapure water to eliminate weakly bound ions and residual acid.

In both cases, samples were quickly transferred to the load-lock and dried via rapid evacuation to 10^{-6} mbar to minimize any further interaction with atmospheric oxygen or moisture before analysis.

2.4. X-ray photoelectron spectroscopy (XPS)

X-ray photoelectron spectroscopy (XPS) measurements were performed using a SPECS EnviroESCA instrument, equipped with a monochromated Al Kα X-ray source ($h\nu$ = 1486.71 eV) was used for photoelectron excitation. Photoelectrons were collected using a Phoibos 160 NAP 1D-DLD hemispherical analyzer. High-resolution core-level spectra were acquired at a pass energy of 20 eV, with a step size of 0.1 eV and a dwell time of 0.3 s per point. Survey spectra (provided in Fig. S3) were recorded at higher pass energy (100 eV) with a step size of 0.5 eV.

The analysis area was defined by a focused X-ray beam of approximately 300 μm in diameter, with sample positioning ensured by a laser-based alignment system.

Operando NAP-XPS measurements with simultaneous chronoamperometric current monitoring were conducted using a custom-built electrochemical NAP-XPS cell at the SPL-HTC infrastructure in Prague, as detailed in Ref. [22]. The cell enables surface-sensitive monitoring of catalyst layers deposited on polymer electrolyte membranes during controlled electrochemical polarization. The complete design and validation of the cell have been reported previously in Ref. [22], while the NiSeTe-specific membrane-supported configuration used in this work is shown in Fig. 1.

The cell was operated in a membrane-supported half-cell configuration, with the NiSeTe catalyst as the working electrode (WE), a Pt wire as the counter electrode (CE), and a hydrogen reference electrode (Gaskatel) as the reference electrode (RE). To maintain membrane hydration and ensure a continuous supply of reagents during polarization, all NAP-XPS experiments were performed at a constant water vapor pressure of 2 mbar. Chemical state assignments and peak fitting parameters are detailed in the Supporting Information. High-resolution core-level spectra were fitted using Shirley-type backgrounds, with chemically constrained spin–orbit splitting, area ratios, and full width at half maximum values as detailed in the Supporting Information.

In this work, the term "operando" is used specifically to describe NAP-XPS measurements performed under applied electrochemical bias while simultaneously recording the chronoamperometric current response of the NiSeTe working electrode. These measurements correlate surface chemical evolution with the electrochemical state of the electrode under HER- and OER-relevant polarization conditions, rather than providing full catalytic performance benchmarking.

2.5. Preparation of membrane-supported NiSeTe working electrodes

Membrane-supported NiSeTe working electrodes were prepared by ultrasonic spray deposition using an ExactaCoat system (SonoTek). The catalyst ink was prepared by dispersing 25 mg of NiSeTe in a 3.5:1 (v/v) H_2O/ethanol mixture and 100 μL of D521 Nafion ionomer solution (5 wt %). The ink was sonicated in an ultrasonic bath for 1 h to ensure homogeneous dispersion. The ink was then deposited directly on NR212 Nafion Proton Exchange Membrane (PEM) (thickness 50.8 μm, Chemours), to achieve a catalyst loading of approximately 0.28 mg cm^{-2} over an active area of 1 × 1 cm^2.

The resulting catalyst-coated membranes were mounted directly in the membrane-supported electrochemical NAP-XPS configuration without hot-pressing or further post-treatment, thereby preserving the initial chemical state of the catalyst surface for bias-controlled operando NAP-XPS measurements. Electrical contact for the catalytic layer was provided by Au TEM grids (Agar Scientific; hole width 420 μm, bar width 80 μm). In the membrane-supported half-cell configuration, the working electrode (NiSeTe) faced the photoelectron detector from the vacuum side, while the counter and reference electrodes on the opposing side of the PEM were immersed in circulating 0.5 M H_2SO_4 within the liquid compartment of the cell.

3. Results and discussion

The chemical reaction of the acid electrolyte is intrinsically confined to the topmost atomic layers of NiSeTe. Consequently, XPS serves as the most direct and mechanistically informative probe to track this surface evolution. The sub-nanometer depth sensitivity of the technique enables us to monitor, with high fidelity, the selective dissolution of native Te oxide species, the elimination of Ni-O(H) environments, and the subsequent reorganization of chalcogen bonding configurations as the surface undergoes acid-induced reconstruction.

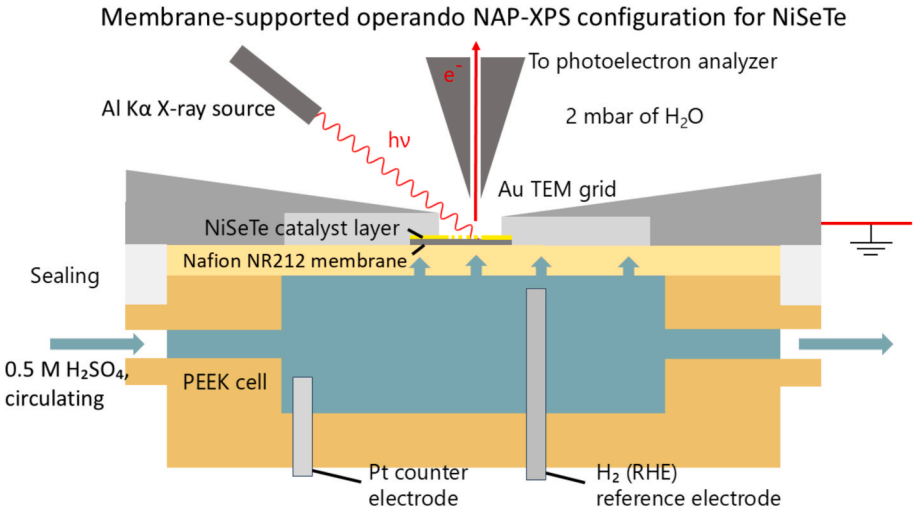

Fig. 1. Schematic of the membrane-supported operando NAP-XPS configuration used for NiSeTe. The NiSeTe catalyst layer on Nafion NR212 faces the analyzer from the vapor side, while the Pt counter electrode and H_2 reference electrode are located in circulating 0.5 M H_2SO_4 on the opposite side. Measurements were performed under 2 mbar H_2O vapor with simultaneous current monitoring.

3.1. Structural and morphological characterization of NiSeTe

The structural layered nature of the NiSeTe single crystals was first established through XRD and SEM prior to any surface chemical analysis. The diffraction pattern (Fig. 2a) exhibits pronounced (00 $\bar{1}$) reflections, specifically the (001) and (002) peaks at 17.5° and 35.2° 2θ respectively. The logarithmic intensity scale further reveals weaker higher-order (003) and (004) basal reflections at approximately 54° and 74° 2θ, respectively, without showing intense additional peaks attributable to secondary crystalline phases, confirming the expected hexagonal P-3 m1 structure with marked preferential orientation along the c-axis. This agrees well with prior crystallographic reports [10,23] of ternary Ni(Se,Te) layered phases and highlights the quasi-two-dimensional character of NiSeTe, where weak van der Waals forces separate chalcogen-Ni-chalcogen trilayers. The XRD analysis confirms phase identification through lattice parameter correspondence with ICOD 00–018-0896 pattern [24]. The sharp peak shapes and absence of secondary reflections indicate high crystalline order and negligible intergrowth of impurity phases.

SEM imaging (Fig. 2b) reveals large, terraced-like features, indicating that the crystals cleave along natural planes rather than fracturing irregularly. The absence of granular roughness or microcracks further supports this interpretation. Corresponding EDS elemental maps confirm a homogeneous distribution of Ni, Se, and Te, see Fig. S1. These results demonstrate that the crystals are structurally uniform and that any surface modifications observed upon acid treatment arise from chemical processes rather than morphological defects or inhomogeneity. This structural baseline is critical when evaluating the subsequent XPS results.

3.2. Electronic and chemical state of pristine NiSeTe

The pristine crystal exhibits a complex but chemically interpretable surface landscape shaped by native oxidation, adsorbed species, and intrinsic chalcogenide bonding. Correlative core levels analysis for these species is analysed simultaneously and continuously to understand the surface reconstruction following exposure to the acidic environment, which we establish via the Te-3d core level which provides the clearest window into this state. As shown in Fig. 3a, two oxidation species features appear in the spectra in the higher binding energy region: a strong component at 577.0 eV, assigned to fully oxidized TeO_2, and a slightly lower-energy band at 574.6 eV, corresponding to substoichiometric TeO_x species ($0 < x < 2$) [25,26]. Their presence is unsurprising given the known tendency of Te to oxidize spontaneously under ambient conditions, forming mixed surface oxides even on freshly cleaved crystals. Alongside these oxidized features, a lower binding energy Te-$3d_{5/2}$ component at 573.4 eV is observed, consistent with reduced Te environments within the NiSeTe lattice [23]. The coexistence of reduced and oxidized tellurium thus reflects a partially oxidized native layer.

We also measured Ni-2p region of pristine NiSeTe which exhibits complex multiplets structure characteristic of Ni-based compounds as indicated in Fig. 3b. This behavior arises from final-state effects and charge-transfer configurations in Ni^{2+} compounds (e.g., NiO and Ni$(OH)_2$), which produce broad envelopes with satellite features ~ 6 eV above the main line [27,28].

It is well established that Ni-2p spectra cannot be interpreted in terms of single binding energies for distinct oxidation states, because of the multiplets splitting and charge transfer effects, overlapping envelopes whose intensity distribution reflects the local chemical environment rather than discrete valence states [29]. In this context, the component centered at 854.1 eV is assigned to Ni coordinated by chalcogen atoms (Ni-Se/Te), consistent with literature values reported for nickel selenides and tellurides while 856.6 eV envelope is conservatively assigned to a mixed Ni-O(H) environment, encompassing contributions from NiO- and $Ni(OH)_2$-like species, rather than to one unique Ni state. Additionally, the components at 859.2 and 861.8 eV are satellites which are diagnostic of Ni-O containing species The accompanying shake-up satellites appearing at 859.2 and 861.8 eV further confirm the oxide/hydroxide origin of this contribution. Furthermore, the O-1 s spectrum does not exhibit a distinct lattice-oxygen feature near ~ 529.5–530.0 eV that would be characteristic of stoichiometric NiO [30,31]. This discrepancy underscores that in disordered or surface-hydroxylated systems, the Ni-2p multiplet structure provides a more reliable diagnostic tool for the metal local environment than the corresponding lattice oxygen signal in O-1 s [33,34]. We analyse O-1 s core level which in principle captures the most prominent oxide surface features of NiSeTe surface. Since we are considering acid treatment in a later stage, oxygen and sulfur core levels together provide a coherent picture of the oxidized surface termination of pristine NiSeTe. The O-1 s spectrum (Fig. 3d) is composed of four chemically distinct components, reflecting

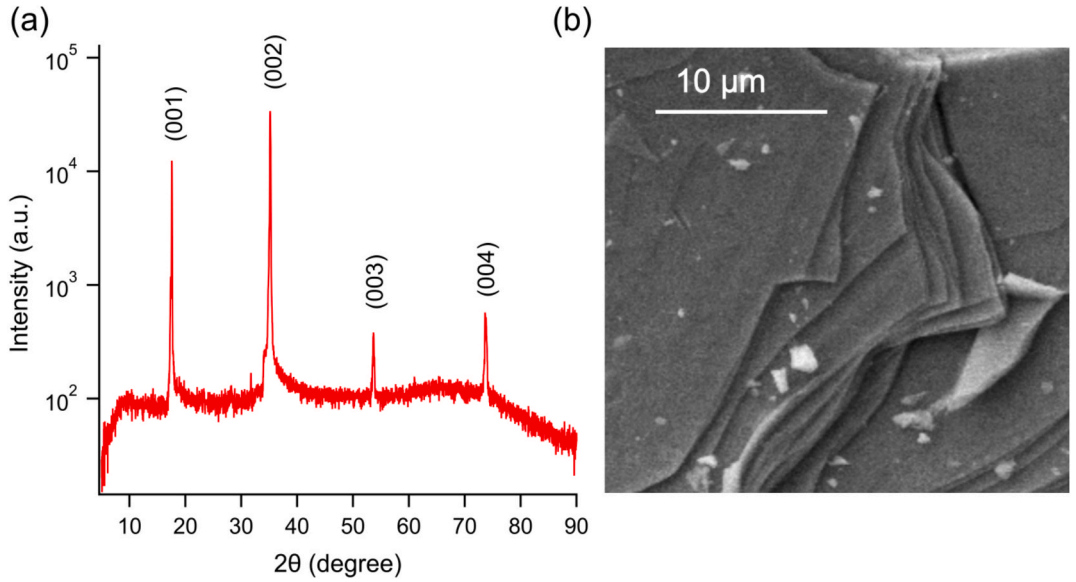

Fig. 2. Structural and morphological characterization of as-synthesized NiSeTe. (a) XRD pattern plotted on a logarithmic intensity scale to enhance the visibility of weak reflections. The dominant (001) and (002) basal reflections, together with weaker higher-order (003) and (004) reflections, confirm the preferential orientation of the layered NiSeTe crystal along the c-axis. (b) SEM image showing the terraced morphology characteristic of the layered crystal surface.

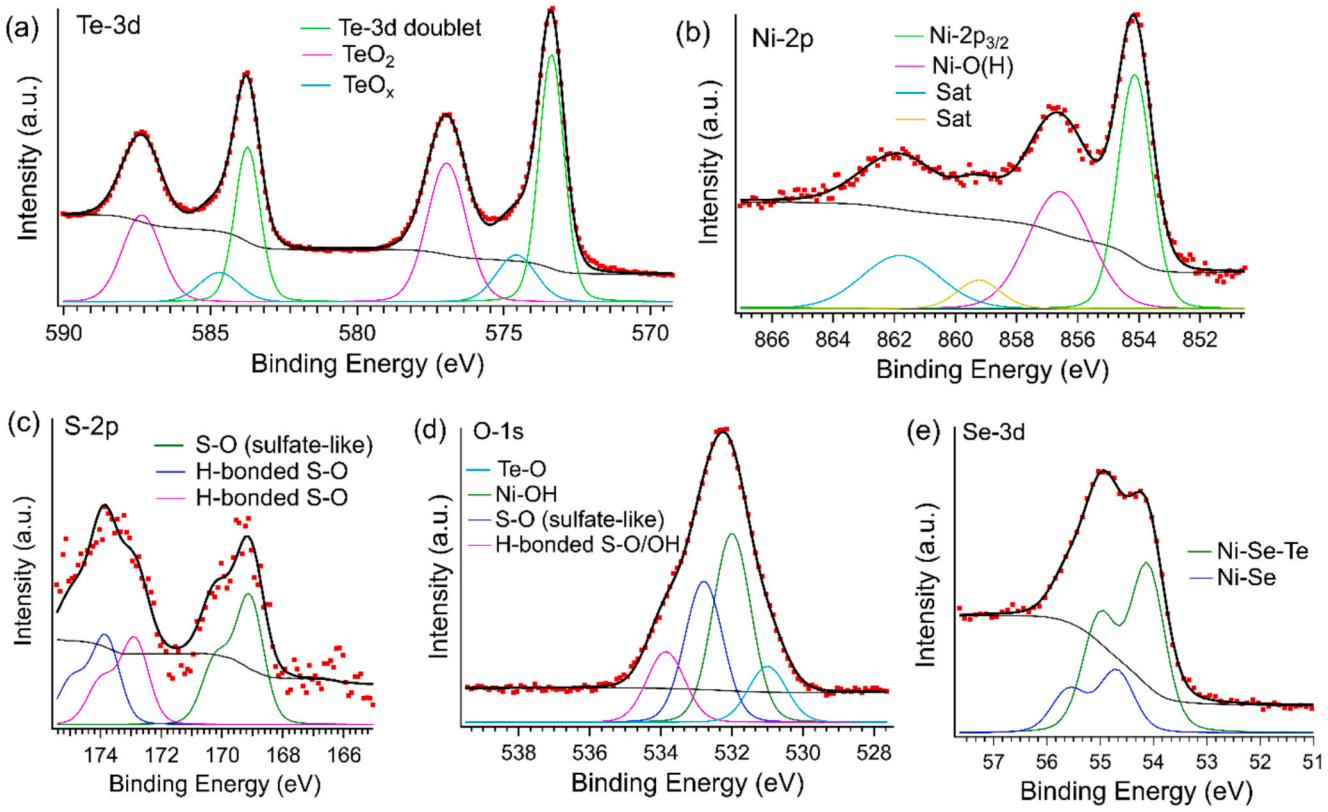

Fig. 3. (a) Te-3d, (b) Ni-2$p_{3/2}$, (c) S-2p, (d) O-1s and (e) Se-3d core levels of NiSeTe pristine crystal.

contributions from native tellurium oxidation, hydroxylated nickel species, and adsorbed sulfur-oxygen groups. The lowest binding energy component at 531.0 eV is assigned to Te-O bonding in TeO_2/TeO_x, consistent with the presence of oxidized tellurium identified independently in the Te-3d region. This assignment is well established for Te oxides on chalcogenide surfaces, where lattice oxygen in TeO_2 appears in the 530.8–531.2 eV range [32,33]. The dominant O-1 s contribution at 532.0 eV (41.4%) is attributed to Ni-OH species, including surface hydroxyls and partially hydroxylated nickel sites formed during ambient exposure.

At higher binding energies, two oxygen components dominate the remaining spectral weight. The peak at 532.8 eV is assigned to oxygen bound in sulfate or bisulfate groups (S-O) chemisorbed at the surface whereas the highest binding energy contribution at 533.9 eV is assigned to H-bonded S-O/OH environments, including hydrogen-bonded sulfate-related oxygen and hydroxylated oxygen species. This assignment is kept distinct from the additional ~ 535.0 eV component observed after acid exposure and washing, which is attributed to H_2O species.[34]. Together, these two components account for nearly half of the total O-1 s intensity, demonstrating that sulfur-oxygen species constitute a major fraction of the pristine surface termination.

This interpretation is strongly corroborated by the S-2p spectrum (Fig. 3c), which reveals three distinct S(VI) doublets with S-2$p_{3/2}$ binding energies at 169.1 eV, 172.8 eV and 173.8 eV. The component at 169.1 eV is characteristic of sulfate or bisulfate species (SO_4^{2-} / HSO_4^-) adsorbed on metal or chalcogenide surfaces [35]. The two higher binding energy components above 172.0 eV are assigned to H-bonded S-O environments within S(VI)-type sulfate/bisulfate species, rather than to sulfite-like S(IV) species. These higher binding energy sulfur environments are distinguishable in S-2p but do not correspond uniquely to a single O-1 s component because the high binding energy O-1 s region also contains overlapping contributions from hydrogen-bonded S-O/OH and hydrated oxygen species. Similar multi-component S(VI) envelopes have been widely reported for sulfate adsorption on oxides and sulfated surfaces and are attributed to variations in hydrogen bonding, protonation state, and surface binding geometry rather than discrete sulfur phases [36].

Importantly, no S-2p features are observed below 168 eV, excluding the presence of sulfide, sulfite, or elemental sulfur [37]. Sulfur therefore exists exclusively in its highest oxidation state in the pristine crystal. The coexistence of multiple S(VI) components in S-2p and their corresponding oxygen contributions in O-1 s indicates a heterogeneous sulfate/bisulfate adlayer accumulated during air exposure or sample handling, rather than sulfur incorporation into the NiSeTe lattice.

One the other hand,the Se-3d region reveals two distinct chalcogenide environments. Peaks at 54.1 eV and 54.7 eV correspond respectively to Se coordinated within the NiSeTe lattice and Se situated in a more Ni-rich local environment akin to that found in NiSe [38].

In summary, the multi-core analysis of Te-3d, Ni-2p, Se-3d, O-1 s and S-2p spectra demonstrate that the pristine NiSeTe surface is terminated by a chemically complex but well-defined oxidized overlayer composed of TeO_2/TeO_x, Ni-OH species, and a heterogeneous population of sulfate/bisulfate groups. This sulfur-oxygen rich termination masks the underlying chalcogenide lattice and plays a decisive role in the subsequent acid-induced reconstruction. The following section tracks how this structurally complex termination evolves under acidity.

3.3. Acid-Induced surface evolution: dissolution and overlayer formation

Exposure of NiSeTe to 0.5 M H_2SO_4 produces an immediate and striking transformation across all core levels, reflecting the intrinsic chemical reactivity of the native oxide-rich termination. The most pronounced change occurs in the Te-3d spectrum. In the pristine surface, more than half of the detected tellurium exists in oxidized form (≈ 31 at. % of the total surface signal, corresponding to 53% of total Te). Upon acid exposure, both TeO_2 and TeO_x components disappear completely. Their removal is not accompanied by the emergence of metallic Te features, but instead by a strong attenuation of the overall Te signal,

leaving only a weak contribution attributable to lattice Te. This behavior confirms that the transformation is chemical rather than reductive. The acid therefore strips the oxidized Te layer while simultaneously reducing the surface sensitive chalcogen signal through overlayer formation.

The O-1 s region provides complementary evidence for this dissolution process. The 531.0 eV Te-O component present in the pristine sample vanishes after acid exposure, consistent with the loss of TeO_2 (Fig. 5b). At the same time, the 532.8 eV is associated with mixed S-O and sulfate-derived oxygen, expands becoming the dominant oxygen contribution. The strong growth of S(VI)-related components indicates that the surface becomes enriched in sulfate/bisulfate species rather than depleted of oxygen overall. The most plausible explanation is that the removal of TeO_2 exposes sites that rapidly bind bisulfate and sulfate species from the acid droplet, forming a highly hydrated S(VI)-rich adlayer.

This evolution is mirrored clearly in the S-2p spectrum. The pristine surface exhibits a triplet of S(VI) components at 169.1, 172.8, and 173.8 eV, typical of heterogeneous sulfate-like environments accumulated under ambient exposure. Upon acid treatment, these collapse into a single dominant peak at 169.6 eV, indicating consolidation into a chemically uniform sulfate/bisulfate termination. The comparative S-2p spectra of the acid-exposed and washed surfaces are provided in Fig. S4.6 and show that acid exposure reorganizes the sulfur chemistry into a more uniform sulfate-like S-O termination. The reduction in spectral multiplicity indicates that the acid exposure removes or reorganizes the weak H-bonded S-O environments present on the pristine surface, leaving a chemically simpler sulfate-like S-O termination, consistent with the dominant sulfate-related O-1 s contribution.

The Ni-2p spectrum undergoes the most drastic restructuring. Both the lattice Ni-Se-Te component at 854.1 eV and the oxide/hydroxide component at 856.6 eV disappear, along with their satellite structures (Fig. 4a). The envelope becomes nearly featureless. This suggests that the acid removes the $NiO/Ni(OH)_2$ layer and destabilizes the uppermost Ni-chalcogenide bonds, either through partial dissolution or by burying the Ni beneath a newly formed sulfate adlayer. Because sulfate carries strong cross sections in O-1 s but virtually none in the Ni-2p region, a thick S(VI) termination would severely attenuate the Ni signal without leaving detectable Ni-related spectral features.

The Se-3d region exhibits substantial attenuation under acid treatment. In the pristine surface, selenium contributes approximately (24 at. %) of the surface composition. Following acid exposure, the Se signal drops to near the detection limit (Fig. 4b). The dramatic loss of Se intensity is most plausibly attributed to surface sensitive attenuation caused by dissolution of the oxide cap and formation of a sulfate-rich overlayer that reduces effective photoelectron escape from deeper chalcogen planes.

These combined observations point to a coherent chemical picture: the acid does not reduce the surface but instead strips away native oxides and replaces them with a dense, disordered sulfate-rich layer. TeO_2 and NiO(H) dissolve first; mixed S(VI) species reorganize; Se and Ni become attenuated; and the underlying NiSeTe lattice becomes partially shrouded. The resulting surface is chemically distinct from both the pristine and washed states and represents a transient restructuring state induced solely by acid chemistry.

The most revealing insights emerge after rinsing the acid-exposed crystal. Washing removes soluble sulfate and bisulfate species but leaves behind stable, tightly bound S(VI) groups and re-exposes the recovered NiSeTe surface (Fig. S4.6). This regeneration becomes evident across all core levels.

In the Te-3d region, the oxide signatures remain absent, confirming that TeO2 and TeOx removal is irreversible (Fig. 4a). The lattice Te contribution re-emerges and now dominates the surface composition (~73 at.% of the detected signal), consistent with removal of both the oxide cap and much of the sulfate overlayer. This recovery supports a model in which washing removes the sulfate overlayer, allowing X-rays to once again reach the chalcogenide planes beneath.

The O-1 s signal decreases substantially after washing, indicating desorption of physisorbed sulfate and water (Fig. 5b). The remaining oxygen is dominated by sulfate-like contributions and minor hydroxyl species. Importantly, the lower binding energy component at 532.0 eV remains approximately at the same binding energy as observed in the pristine sample. However, RSF-corrected Ni-2p quantification shows that the NiOH contribution (~5 at.% in the pristine state) is eliminated after acid exposure and does not recover upon washing. The absence of Ni-O(H) satellites in Ni-2p confirms that the original NiO(H) phase is not reformed. Therefore, the persisting 532.0 eV O-1 s component after washing is more plausibly assigned to surface hydroxyl species or defect-associated oxygen on the reconstructed NiSeTe termination rather than to a stoichiometric NiOH overlayer. The simultaneous presence of a feature at 535.0 eV, characteristic of adsorbed water, further supports a hydrated surface environment in which isolated –OH groups can form without regenerating a bulk NiO(H) phase.

The comparative S-2p spectra in Fig. S4.6 provide diagnostic support for the residual sulfate-derived termination after washing. After washing, two sulfate-derived peaks reappear at 168.9 eV and 169.6 eV. These values lie remarkably close to the pristine 169.1 eV component, implying that the washed surface retains a stable, chemisorbed sulfate layer comparable in composition but not identical to the native atmospheric sulfur-oxygen groups. The higher-order S(VI) components at 172.0–174.0 eV, however, do not return, meaning the acid and wash sequence removes the weakly bound sulfur environments present on the pristine surface. The remaining O-1 s intensity at high binding energy is therefore assigned to overlapping H-bonded S-O/OH and H_2O

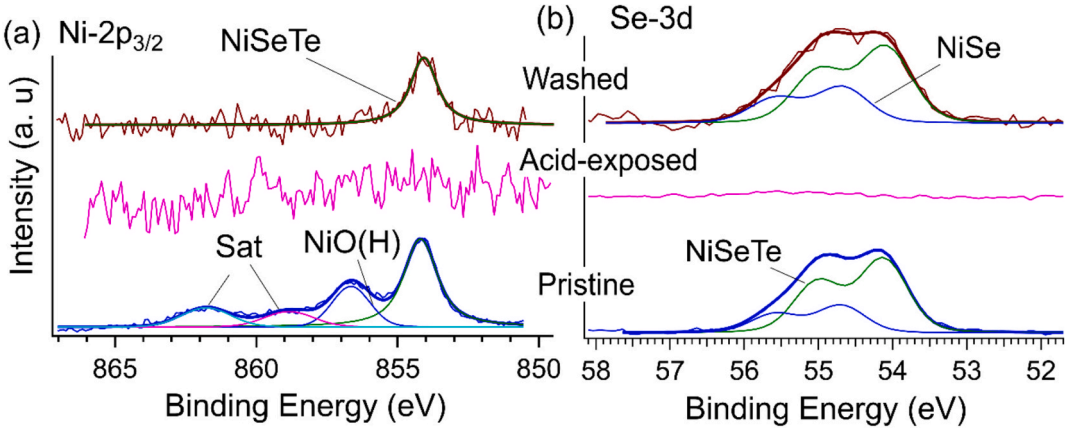

Fig. 4. (a) Te-3d and (b) Se-3d core levels of pristine, acid-exposed and washed NiSeTe crystal.

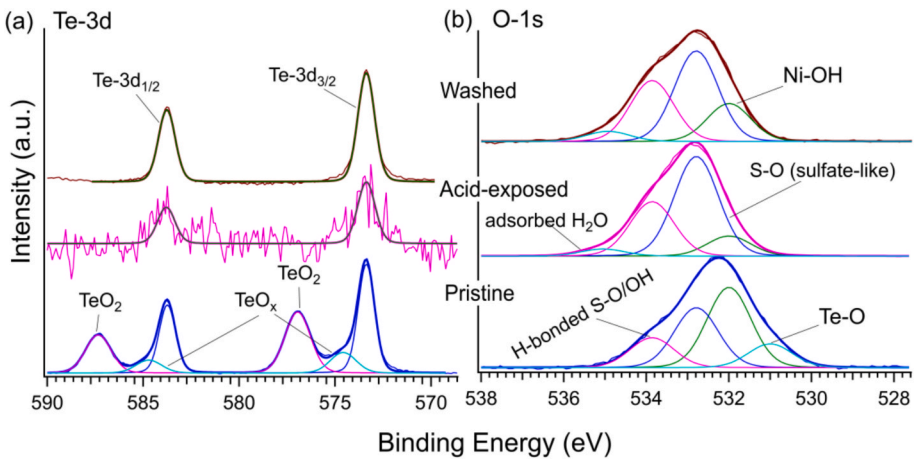

Fig. 5. (a) Te-3d and (b) O-1s core levels of pristine, acid exposed and washed NiSeTe crystal.

contributions.

Selenium partially reappears after washing with almost the same atomic concentration as in the pristine crystal (~23 at. %), supporting a model in which the acid-induced attenuation was primarily overlayer-driven rather than complete selenium dissolution. The two lattice components at 54.1 eV and 54.7 eV return with essentially the same energy separation as before, demonstrating that the acid-treated surface has not undergone irreversible compositional alteration within the detectable subsurface region. The attenuation in area is explained by the persistence of the S(VI) overlayer, which partially obscures the chalcogenide lattice beneath.

Nickel remains detectable but strongly attenuated (~ 4 at.%), consistent with its deeper position and lower escape depth relative to Te and Se.

Taken together, the washed-state spectra reveal a surface that has been chemically reset. The oxidized Te and Ni layers are gone; the chalcogenide lattice is again visible; and only a thin, stable sulfate adlayer persists. This final state is chemically simpler, more uniform, and electronically cleaner than the pristine surface and therefore has significant implications for both catalysis and the preservation of topologically relevant surface states.

To examine whether acid treatment induces any structural or compositional degradation beyond the surface sensitive changes detected by XPS, we conducted SEM and EDS on the washed crystal. The SEM results revealed no visible surface degradation, as shown in Fig. S2.1. Similarly, the EDS spectra before and after the acid treatment were comparable (Fig. S2.2). We conclude that the transformations induced by the acid, as detected by XPS, correspond to surface-localized chemical reconstruction rather than bulk dissolution or destructive etching. This distinction is significant because it is the surface restructuring, rather than any morphological changes, that influences the electrocatalytic behavior in chalcogenides.

Additionally, RSF-corrected quantification trend confirms that the pristine surface contains approximately 31 at. % oxidized tellurium ($TeO_2 + TeO_x$), corresponding to ~ 53% of the total Te signal, and ~ 5 at. % NiOH (~28% of total Ni) (Table S4.1 and Table S4.2). Acid exposure eliminates these oxide components entirely while strongly attenuating both Ni and Se intensities due to the formation of a sulfate-rich overlayer. After washing, the surface becomes dominated by lattice Te (~73 at. % of the detected signal), while selenium returns to approximately its pristine relative atomic fraction (~23 at. %). Importantly, although the normalized Se concentration remains similar, its absolute photoelectron intensity decreases, indicating attenuation rather than stoichiometric enrichment. Nickel strongly suppressed (~ 4 at. %), consistent with its lower escape depth and sensitivity to overlayer coverage.

3.4. Operando NAP-XPS with simultaneous current monitoring: distinguishing bias-induced effects from chemical surface evolution

To disentangle potential-induced electrostatic effects from true chemical changes in the NAP-XPS data, special care must be taken because absolute binding energies in operando NAP-XPS measurements can be strongly influenced by the local electric potential at the electrode–electrolyte interface, particularly when a hydrated polymer electrolyte such as Nafion is present together with a catalyst ink layer [39,40]. Apparent shifts of core level binding energies with applied potential have been widely observed in operando/ambient-pressure XPS studies of electrochemical systems and are understood to arise primarily from the electrostatic potential drop across the electrolyte and interface, rather than purely from intrinsic chemical oxidation states. Nevertheless, qualitative analysis based on core level line shapes and relative intensity evolution provides a reliable approach for monitoring genuine chemical changes under electrochemical bias.

Simultaneous chronoamperometric current–time responses were recorded during the operando NAP-XPS measurements to verify electrochemical polarization of the NiSeTe working electrode during spectral acquisition (Fig. 6c,d). Under HER-relevant cathodic potentials, stable negative currents were observed, with the largest cathodic response at - 0.20 V. Under OER-relevant anodic potentials, positive currents were recorded at both 1.50 and 1.80 V, with the larger response at 1.80 V and a gradual current decay consistent with surface oxidation or passivation. These traces confirm that the NAP-XPS spectra were collected under active electrochemical bias, while the chemical interpretation remains based on the evolution of core-level line shapes and relative intensities.

Under HER-relevant cathodic polarization, the Te-3d line shape remains essentially unchanged as shown in Fig. 6a, while simultaneous current monitoring confirms stable cathodic response during spectral acquisition (Fig. 6c). No new high binding energy components attributable to Te-O bonding are observed, and the relative intensity of reduced Te species remains constant within experimental uncertainty. This behavior indicates that the tellurium surface is already in a reduced, oxide-free state prior to bias application, consistent with the acid-induced removal of native TeO_2 identified on the single crystal surface. Importantly, the absence of further Te-3d line-shape evolution under cathodic polarization indicates that, once Te-oxide species have been chemically removed by sulfuric acid exposure, the applied HER-relevant bias does not induce additional detectable Te reduction under the present measurement conditions.

In contrast, anodic polarization at 1.50 and 1.80 V vs RHE produces positive current responses (Fig. 6d) and leads to the emergence of higher-binding energy Te-3d components consistent with reoxidized

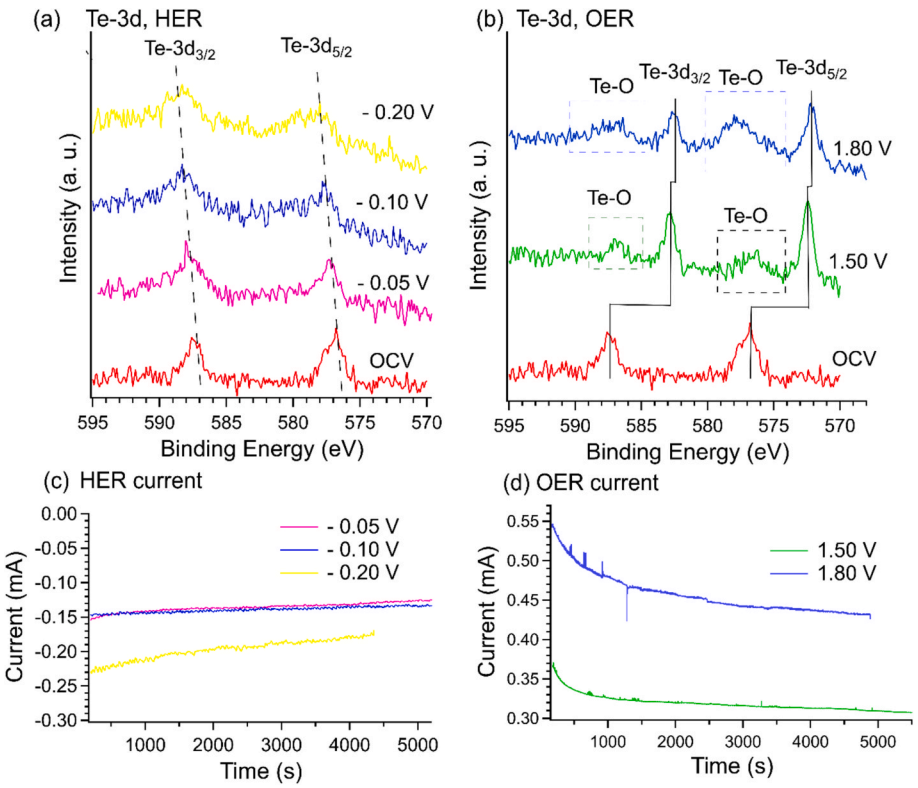

Fig. 6. Operando NAP-XPS measurements with simultaneous chronoamperometric monitoring under HER- and OER-relevant polarization. Te-3d spectra collected under (a) cathodic HER-relevant and (b) anodic OER-relevant potentials. Corresponding current–time responses recorded during spectral acquisition under (c) cathodic potentials of - 0.05, - 0.10, and - 0.20 V and (d) anodic potentials of 1.50 and 1.80 V. All potentials are reported versus RHE.

TeO_x/TeO_2 species (Fig. 6b).

The larger apparent binding energy shifts observed under OER-relevant anodic polarization compared with HER-relevant cathodic polarization are attributed to anodic formation of an insulating surface oxide layer, which reduces electronic screening and weakens electrical coupling to the grounded current collector, causing a greater fraction of the applied potential to drop locally at the catalyst-electrolyte interface rather than being efficiently dissipated through the metallic catalyst, as commonly observed in operando AP-XPS of oxide-forming electrodes [39,41].

Crucially, the line shape evolution of the Te-3d spectra, rather than the absolute energy position, provides the chemically meaningful information. The appearance of broad, asymmetric high energy components under anodic bias is consistent with oxygen incorporation into tellurium surface sites and the re-formation of TeO_x species. Furthermore, the corresponding Se-3d and Ni-2p operando spectra (Fig. S5.1 and Fig. S5.2) support this interpretation. Se exhibits larger apparent binding energy shifts under OER (~5 eV) than HER (~1 eV), yet without clear SeO_x formation. In contrast, Ni-2p line shape does not change under HER, however, it is strongly attenuated under anodic bias, consistent with growth of an insulating surface oxide that suppresses Ni photoelectrons.

These observations confirm that cathodic bias does not induce a new chemical oxidation state of NiSeTe surface under the present HER-relevant conditions, whereas anodic polarization promotes oxidative reconstruction of tellurium at the outermost surface. Above all, the consistent absence of Te-O under HER-relevant polarization and its reappearance under OER-relevant polarization therefore remains a robust indicator of bias-dependent surface evolution.

The operando NAP-XPS results reinforce the central mechanistic picture established from the single crystal study: acid exposure alone is sufficient to remove native Te oxides and generate an oxide-free NiSeTe surface, while anodic bias primarily governs re-oxidation kinetics rather than reduction. Thus, the combined spectroscopic and electrochemical response separates acid-driven chemical reconstruction from bias-induced surface oxidation.

4. Conclusion

This work demonstrates that NiSeTe single crystals undergo a substantial, yet chemically controlled, surface reconstruction upon exposure to acidic media. By combining systematic multi-core XPS analysis (Te-3d, Se-3d, Ni-2p, O-1 s and S-2p) with complementary SEM/EDS and operando NAP-XPS measurements coupled to simultaneous chronoamperometric monitoring, we have established a coherent reconstruction pathway, driven primarily by chemical reactions at the outermost atomic layers, rather than by electrochemical reduction.

In its pristine state, the NiSeTe surface is dominated by TeO_2/TeO_x species, Ni-O(H) groups, and a heterogeneous adlayer of oxidized sulfur species, which collectively obscure the underlying chalcogenide lattice. Acid exposure, even in the absence of any applied potential, rapidly removes both TeO_2 and Ni-O(H) layers through chemical dissolution, while simultaneously reorganizing sulfur-oxygen species into sulfate/bisulfate-rich adlayer.

Subsequent rinsing removes weakly bound sulfate species while preserving a thin, chemisorbed S(VI) layer, revealing a chemically simplified and oxide-free NiSeTe termination. In this “reset” state, lattice-derived Te and Se signals are recovered, Ni-chalcogenide coordination dominates the Ni-2p spectrum, and no reformation of Te oxides or Ni hydroxides is detected. The resulting surface is therefore closer to the intrinsic Ni-Se-Te bonding environment than the native, air-exposed crystal.

Operando NAP-XPS measurements with simultaneous current monitoring further support this interpretation. Under cathodic potentials relevant to the hydrogen evolution reaction (HER), no additional Te reduction is detected under the present HER-relevant conditions,

indicating that the acid-reconstructed surface is already oxide-free before cathodic polarization. Conversely, OER-relevant anodic polarization produces positive current responses and induces a partial reoxidation of tellurium, manifested as Te-O spectral broadening, while large apparent binding energy shifts are shown to arise predominantly from electrostatic potential drops across the Nafion-based electrode architecture rather than from intrinsic chemical changes.

Collectively, these results clarify that many surface activation phenomena previously attributed to electrochemical reduction in Ni/Te-based electrocatalysts are instead explained by acid-driven chemical cleaning and surface reorganization. The reconstructed, post-washed surface represents a chemically stable and electronically cleaner termination that preserves the intrinsic electronic structure of NiSeTe. More broadly, this work highlights the necessity of disentangling chemical surface reconstruction from electrochemical effects and establishes controlled acid treatments as a reliable, reproducible route to preparing well-defined oxide-free surfaces for both catalytic and electronic studies of transition metal chalcogenides.

CRediT authorship contribution statement

Ashraf Abdelrahman Assadig Elameen: Writing – review & editing, Writing – original draft, Visualization, Validation, Methodology, Investigation, Data curation, Conceptualization. **Tomáš Hrbek:** Writing – review & editing, Validation, Resources, Methodology, Investigation, Data curation, Conceptualization. **Yevheniia Lobko:** Writing – review & editing, Validation, Resources, Methodology, Investigation, Data curation. **Viacheslav Kalinovych:** Validation, Methodology, Data curation. **Angelica Chiodoni:** Supervision, Project administration, Funding acquisition. **Micaela Castellino:** Writing – review & editing, Writing – original draft, Validation, Supervision, Project administration. **Peter Kúš:** Writing – review & editing, Validation, Resources, Methodology, Investigation, Data curation. **Rui Gusmão:** Writing – review & editing, Validation, Resources, Funding acquisition, Data curation. **Zdenek Sofer:** Writing – review & editing, Resources, Project administration, Funding acquisition. **Andrea Lamberti:** Supervision, Project administration, Funding acquisition.

Declaration of competing interest

The authors declare the following financial interests/personal relationships which may be considered as potential competing interests: Ashraf Abdelrahman Assadig Elameen reports financial support, equipment, drugs, or supplies, and travel were provided by CERIC Laboratory. If there are other authors, they declare that they have no known competing financial interests or personal relationships that could have appeared to influence the work reported in this paper.

Acknowledgements

This publication is part of the project PNRR-NGEU which has received funding from the MUR-DM118/2023. The authors acknowledge CERIC-ERIC Consortium for access to experimental facilities at LRI SPL-HTC in Prague (Proposal number: 20252027). R. G. acknowledges funding from the Czech Science Foundation (GAČR project No. 26-22647S). Z.S. was supported by the financial support by the ERC-CZ program (Project No. LL2101) and by the project Advanced Functional Nanorobots (reg. No. CZ.02.1.01/0.0/0.0/15_003/0000444 financed by the EFRR).

Appendix A. Supplementary data

Supplementary data to this article can be found online at https://doi.org/10.1016/j.apsusc.2026.167652.

Data availability

Data will be made available on request.

References

[1] Y. Liu, Y. Guo, Y. Liu, Z. Wei, K. Wang, Z. Shi, A mini review on transition metal chalcogenides for electrocatalytic water splitting: bridging material design and practical application, Energy Fuel 37 (2023) 2608–2630, https://doi.org/10.1021/acs.energyfuels.2c03833.
[2] D. Gao, B. Xia, C. Zhu, Y. Du, P. Xi, D. Xue, J. Ding, J. Wang, Activation of the $MoSe_2$ basal plane and Se-edge by B doping for enhanced hydrogen evolution, J. Mater. Chem. A Mater. 6 (2018) 510–515, https://doi.org/10.1039/C7TA09982G.
[3] H. Xu, J. Cao, C. Shan, B. Wang, P. Xi, W. Liu, Y. Tang, MOF-derived hollow CoS decorated with CeO_x nanoparticles for boosting oxygen evolution reaction electrocatalysis, Angew. Chem. 130 (2018) 8790–8794, https://doi.org/10.1002/ange.201804673.
[4] X. Ji, Y. Lin, J. Zeng, Z. Ren, Z. Lin, Y. Mu, Y. Qiu, J. Yu, Graphene/MoS_2/FeCoNi(OH)x and Graphene/MoS_2/FeCoNiPx multilayer-stacked vertical nanosheets on carbon fibers for highly efficient overall water splitting, Nat. Commun. 12 (2021) 1380, https://doi.org/10.1038/s41467-021-21742-y.
[5] X. Xu, F. Song, X. Hu, A nickel iron diselenide-derived efficient oxygen-evolution catalyst, Nat. Commun. 7 (2016) 12324, https://doi.org/10.1038/ncomms12324.
[6] L. Yang, L. Huang, Y. Yao, L. Jiao, In-situ construction of lattice-matching NiP_2/$NiSe_2$ heterointerfaces with electron redistribution for boosting overall water splitting, Appl. Catal. B 282 (2021) 119584, https://doi.org/10.1016/j.apcatb.2020.119584.
[7] V. Vij, S. Sultan, A.M. Harzandi, A. Meena, J.N. Tiwari, W.-G. Lee, T. Yoon, K. S. Kim, Nickel-based electrocatalysts for energy-related applications: oxygen reduction oxygen evolution, and hydrogen evolution reactions, ACS Catal. 7 (2017) 7196–7225, https://doi.org/10.1021/acscatal.7b01800.
[8] A.T. Swesi, J. Masud, M. Nath, Nickel selenide as a high-efficiency catalyst for oxygen evolution reaction, Energy Environ. Sci. 9 (2016) 1771–1782, https://doi.org/10.1039/C5EE02463C.
[9] U. De Silva, J. Masud, N. Zhang, Y. Hong, W.P.R. Liyanage, M. Asle Zaeem, M. Nath, Nickel telluride as a bifunctional electrocatalyst for efficient water splitting in alkaline medium, J. Mater. Chem. A Mater. 6 (2018) 7608–7622, https://doi.org/10.1039/C8TA01760C.
[10] I.M. Abdullahi, S. Thomas, A. Gagliardi, M.A. Zaeem, M. Nath, Nanostructured ternary nickel-based mixed anionic (telluro)-selenide as a superior catalyst for oxygen evolution reaction, Energ. Technol. 11 (2023), https://doi.org/10.1002/ente.202300177.
[11] Y.-X. Yuan, L. Pan, Z.-Q. Wang, Z.-Y. Zeng, H.-Y. Geng, X.-R. Chen, Two-dimensional Janus pentagonal MSeTe (M = Ni, Pd, Pt): promising water-splitting photocatalysts and optoelectronic materials, PCCP 25 (2023) 26152–26163, https://doi.org/10.1039/D3CP02398B.
[12] A. Abdelrahman Assadig Elameen, R. Mahjoub Yahia Elhassan, Influence of surface oxidation on the catalytic activity of topological quantum materials, PCCP 27 (2025) 12112–12118, https://doi.org/10.1039/D5CP01040C.
[13] F. Hou, D. Zhang, P. Sharma, S. Singh, T. Wu, J. Seidel, Oxidation kinetics of WTe_2 surfaces in different environments, ACS Appl. Electron. Mater. 2 (2020) 2196–2202, https://doi.org/10.1021/acsaelm.0c00380.
[14] F. Ye, J. Lee, J. Hu, Z. Mao, J. Wei, P.-X.-L. Feng, Environmental instability and degradation of single- and few-layer WTe_2 nanosheets in ambient conditions, Small 12 (2016) 5802–5808, https://doi.org/10.1002/smll.201601207.
[15] X. Chia, Z. Sofer, J. Luxa, M. Pumera, Unconventionally layered $CoTe_2$ and $NiTe_2$ as electrocatalysts for hydrogen evolution, Chem.– A Eur. J. 23 (2017) 11719–11726, https://doi.org/10.1002/chem.201702753.
[16] P. Guo, S. Cao, Y. Wang, X. Lu, Y. Zhang, X. Xin, X. Chi, X. Yu, I. Tojiboyev, H. Salari, A.J. Sobrido, M. Titirici, X. Li, Surface self-reconstruction of telluride induced by in-situ cathodic electrochemical activation for enhanced water oxidation performance, Appl. Catal. B 310 (2022) 121355, https://doi.org/10.1016/j.apcatb.2022.121355.
[17] J.C. McGlynn, T. Dankwort, L. Kienle, N.A.G. Bandeira, J.P. Fraser, E.K. Gibson, I. Cascallana-Matías, K. Kamarás, M.D. Symes, H.N. Miras, A.Y. Ganin, The rapid electrochemical activation of MoTe2 for the hydrogen evolution reaction, Nat. Commun. 10 (2019) 4916, https://doi.org/10.1038/s41467-019-12831-0.
[18] A. Vijayan, N. Sandhyarani, Enhancing the catalytic activity of bulk MoS_2 towards hydrogen evolution reaction by the formation of MoS_2-MoO_3-Re_2O_7 heterostructure, J. Colloid Interface Sci. 623 (2022) 819–831, https://doi.org/10.1016/j.jcis.2022.05.107.
[19] R.S. Datta, F. Haque, M. Mohiuddin, B.J. Carey, N. Syed, A. Zavabeti, B. Zhang, H. Khan, K.J. Berean, J.Z. Ou, N. Mahmood, T. Daeneke, K. Kalantar-zadeh, Highly active two dimensional α-MoO_{3-x} for the electrocatalytic hydrogen evolution reaction, J. Mater. Chem. A Mater. 5 (2017) 24223–24231, https://doi.org/10.1039/C7TA07705J.
[20] Y. Xiang, K. Xiong, L. Yu, H. Zhang, J. Chen, M. Xia, Tuning of crystal phase of nickel telluride nanosheets to construct superior electrocatalyst for hydrogen evolution, J. Alloys Compd. 891 (2022) 161955, https://doi.org/10.1016/j.jallcom.2021.161955.
[21] R.J. Bouchard, The preparation of single crystals of FeS_2, CoS_2, and NiS_2 pyrites by chlorine transport, J. Cryst. Growth 2 (1968) 40–44, https://doi.org/10.1016/0022-0248(68)90067-5.

[22] T. Hrbek, P. Kúš, M.G. Rodríguez, V. Matolín, I. Matolínová, Operando X-ray photoelectron spectroscopy cell for water electrolysis: a complete picture of iridium electronic structure during oxygen evolution reaction, Int. J. Hydrogen Energy 57 (2024) 187–197, https://doi.org/10.1016/j.ijhydene.2023.12.216.
[23] I. Vobornik, A.B. Sarkar, L. Zhang, D.W. Boukhvalov, B. Ghosh, L. Piliai, C. Kuo, D. Mondal, J. Fujii, C.S. Lue, M. Vorokhta, H. Xing, L. Wang, A. Agarwal, A. Politano, Kitkaite NiTeSe, an ambient-stable layered dirac semimetal with low-energy Type-II fermions with application capabilities in spintronics and optoelectronics, Adv. Funct. Mater. 31 (2021), https://doi.org/10.1002/adfm.202106101.
[24] T.A. Häkli, Y. Vuorelainen, T.G. Sahama, Kitkaite (NiTeSe), a new mineral from Kuusamo, northeast Finland, Am. Mineral.: J. Earth Planet. Mater. 50 (1965) 581–586.
[25] B. Chen, H. Sahin, A. Suslu, L. Ding, M.I. Bertoni, F.M. Peeters, S. Tongay, Environmental changes in $MoTe_2$ excitonic dynamics by defects-activated molecular interaction, ACS Nano 9 (2015) 5326–5332, https://doi.org/10.1021/acsnano.5b00985.
[26] J. Luxa, P. Vosecký, V. Mazánek, D. Sedmidubský, M. Pumera, P. Lazar, Z. Sofer, Layered transition-metal ditellurides in electrocatalytic applications—contrasting properties, ACS Catal. 7 (2017) 5706–5716, https://doi.org/10.1021/acscatal.7b02080.
[27] A.P. Grosvenor, M.C. Biesinger, R.St.C. Smart, N.S. McIntyre, New interpretations of XPS spectra of nickel metal and oxides, Surf. Sci. 600 (2006) 1771–1779, https://doi.org/10.1016/j.susc.2006.01.041.
[28] P.S. Bagus, C.J. Nelin, S.T. Mergelsberg, N. Lahiri, E.S. Ilton, Chemical information from XPS: theory and experiment for Ni(OH)2, J. Chem. Phys. 161 (2024), https://doi.org/10.1063/5.0229962.
[29] M.C. Biesinger, B.P. Payne, A.P. Grosvenor, L.W.M. Lau, A.R. Gerson, R.St.C. Smart, Resolving surface chemical states in XPS analysis of first row transition metals, oxides and hydroxides: Cr, Mn, Fe, Co and Ni, Appl. Surf. Sci. 257 (2011) 2717–2730. DOi: 10.1016/j.apsusc.2010.10.051.
[30] M.A. Peck, M.A. Langell, Comparison of nanoscaled and bulk NiO structural and environmental characteristics by XRD, XAFS, and XPS, Chem. Mater. 24 (2012) 4483–4490, https://doi.org/10.1021/cm300739y.
[31] K.J. Gaskell, A. Starace, M.A. Langell, $ZnxNi_{1-x}O$ rocksalt oxide surfaces: novel environment for Zn^{2+} and its effect on the NiO band structure, J. Phys. Chem. C 111 (2007) 13912–13921, https://doi.org/10.1021/jp073590x.
[32] H. Kong, J.-B. Yeo, H.-Y. Lee, A Study on the properties of tellurium-oxide thin films based on the variable sputtering gas ratio, J. Korean Phys. Soc. 66 (2015) 1744–1749, https://doi.org/10.3938/jkps.66.1744.
[33] N. Berchenko, R. Vitchev, M. Trzyna, R. Wojnarowska-Nowak, A. Szczerbakow, A. Badyla, J. Cebulski, T. Story, Surface oxidation of SnTe topological crystalline insulator, Appl. Surf. Sci. 452 (2018) 134–140, https://doi.org/10.1016/j.apsusc.2018.04.246.
[34] M. Wahlqvist, A. Shchukarev, XPS spectra and electronic structure of group IA sulfates, J. Electron Spectros. Relat. Phenomena 156–158 (2007) 310–314, https://doi.org/10.1016/j.elspec.2006.11.032.
[35] P. Ganesan, A. Sivanantham, S. Shanmugam, Inexpensive electrochemical synthesis of nickel iron sulphides on nickel foam: super active and ultra-durable electrocatalysts for alkaline electrolyte membrane water electrolysis, J. Mater. Chem. A Mater. 4 (2016) 16394–16402, https://doi.org/10.1039/C6TA04499A.
[36] S. Tresintsi, K. Simeonidis, N. Pliatsikas, G. Vourlias, P. Patsalas, M. Mitrakas, The role of SO_4^{2-} surface distribution in arsenic removal by iron oxy-hydroxides, J. Solid State Chem. 213 (2014) 145–151, https://doi.org/10.1016/j.jssc.2014.02.026.
[37] D.W. Boukhvalov, G. D'Olimpio, T. Dadiani, J. Sharma, A. Abdelrahman Assadig Elameen, S. Zenone, M. Rosmus, B. Gürbulak, E. Çepni, E. Llobet, E. Magnano, F. Bondino, S. Duman, A. Politano, Self-assembled gallium sulfide (GaS) heterostructures enabling efficient water splitting and selective ammonia sensing, Adv. Funct. Mater. 35 (2025), https://doi.org/10.1002/adfm.202507388.
[38] W. Shi, X. Zhang, G. Che, Hydrothermal synthesis and electrochemical hydrogen storage performance of porous hollow NiSe nanospheres, Int. J. Hydrogen Energy 38 (2013) 7037–7045, https://doi.org/10.1016/j.ijhydene.2013.03.145.
[39] M.F. Lichterman, M.H. Richter, B.S. Brunschwig, N.S. Lewis, H.-J. Lewerenz, Operando X-ray photoelectron spectroscopic investigations of the electrochemical double layer at Ir/KOH(aq) interfaces, J. Electron Spectros. Relat. Phenomena 221 (2017) 99–105, https://doi.org/10.1016/j.elspec.2017.03.011.
[40] N.L. Tran Pham, S. Qian, T. Götsch, C. Grön, J.J. Velasco-Vélez, B.M. Stühmeier, A. Knop-Gericke, H.A. Gasteiger, M. Piana, Elucidating the hydrogen selectivity of $Pt/TiO_x/C$ as a fuel-cell catalyst by operando near-ambient-pressure XPS, ACS Appl. Mater. Interfaces 17 (2025) 50626–50638, https://doi.org/10.1021/acsami.5c09047.
[41] L. Yu, Y. Takagi, T. Nakamura, O. Sekizawa, T. Sakata, T. Uruga, M. Tada, Y. Iwasawa, G. Samjeské, T. Yokoyama, Non-contact electric potential measurements of electrode components in an operating polymer electrolyte fuel cell by near ambient pressure XPS, PCCP 19 (2017) 30798–30803, https://doi.org/10.1039/C7CP05436J.